Results in Engineering 27 (2025) 106557

Contents lists available at ScienceDirect

Results in Engineering

journal homepage: www.sciencedirect.com/journal/results-in-engineering

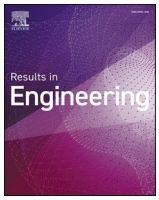

Numerical modelling of tsunami-induced scour around a coastal dike

Ravindra Jayaratne [a,*], Adewale Abimbola [a], Nilakshan Balasubramaniam [a], Mohammad Tabasi [b]

[a] Department of Engineering & Construction, School of Architecture, Computing and Engineering, University of East London, Docklands Campus, 4-6 University Way, London E16 2RD, UK
[b] Technical Research Institue, Fudo Tetra Corporation, Tsuchiura, Japan

ARTICLE INFO

Keywords:
Coastal dikes
Numerical modelling
Tsunami-induced scour
Hydro-sedimentary dynamics
The 2011 Tohoku tsunami
Reynolds-Averaged Navier-Stokes (RANS) modelling
k-ε turbulence model

ABSTRACT

Coastal dikes are vital flood defence structures protecting nearshore from tsunamis, storm surges and extreme waves. However, the physical presence of a coastal structure can impact the hydro-sedimentary dynamics of the nearshore environment. Post-tsunami field surveys of the 2011 Tohoku tsunami indicated that the scour was the most dominant failure mode. When the overtopping plunging jet creates a scour hole in the leeward side of the structure, it causes structural failure in conjunction with other forces acting on the structure. This novel study focuses on 2D numerical model with RANS modelling approach of tsunami-like wave propagation and its associated scour process at the leeward of a coastal dike, obtained from turbulence-averaged Eulerian two-phase flow equations with the kinetic theory of granular flows for inter-granular stress models and a k-ε turbulence model. The numerical model results were validated using tsunami-induced scour laboratory data of 1:50 scale dike models. The results indicated good agreement with the predicted scour depths which were associated with the hydraulic conditions, sediment characteristics, and structure geometry. The current study will be beneficial in determining the compliance of predictive models with the experimental data and numerical analysis, which in turn can be used for validation of other models.

1. Introduction

Coastal areas are vital regions for human recreational activities, tourism, habitat development and economy. These areas get damaged during natural hazards like storm surges or an event of a tsunami. Storm surges are usually caused by hurricanes or storms resulting in sea level rise and consequently flooding coastal regions, damaging infrastructure as well as causing loss of lives. Tsunamis are extremely large waves which are generally generated by subsea phenomena like earthquakes, landslides, volcanic eruptions or even by manmade explosions [1,2]. The Indian Ocean tsunami in 2004, generated by an earthquake resulted in >228,898 casualties, damaging 153,704 houses while the 2011 Tohoku tsunami, which was also generated due to an earthquake, resulted in >15,899 casualties [3,4].

Coastal dikes are mostly common coastal defence structures that can be found in many tsunami-prone areas. They have been successful in protecting the coastal communities and valuable coastal assets in events like storm surges, high tides and tsunamis [3]. However, the physical presence of a structure in the coastal area will have a significant effect on the hydro-sedimentary dynamics in the neighbouring coastal area. Further, a phenomenon like wave overtopping over these defence structures will cause local erosion, also called scour. Scour can directly affect the stability of the structure, damage infrastructure or impact people on the landward side [5].

Tsunami-induced scour is a phenomenon occurring in the coastal region under the influence of tsunami waves. This occurs when the soil layer from the coastal bed/nearshore region gets eroded by tsunami waves. This action in particular, among other factors influencing, can cause significant threats to the stability of structures like buildings, bridges, coastal defence structures and even marine pipelines. In recent years, the studies on tsunamis, and tsunami-induced scour are getting more and more attention from researchers because of the complex nature and severity of the effect on these structures [6–8].

Post-tsunami field surveys after the 1992 Nicaragua tsunami and the 1998 Papua New Guinea found that there were significant levels of scour around structures [9]. This scour is often connected to the main failure mechanisms of structures during the tsunami event [9]. Similar field surveys after the 2011 Tohoku tsunami also confirmed that the

* Corresponding author.
E-mail addresses: r.jayaratne@uel.ac.uk (R. Jayaratne), N.Balasubramaniam@uel.ac.uk (N. Balasubramaniam), tabasi.mohammad@fudotetra.co.jp (M. Tabasi).

https://doi.org/10.1016/j.rineng.2025.106557
Received 24 April 2025; Received in revised form 20 July 2025; Accepted 31 July 2025
Available online 5 August 2025

tsunami-induced scour around the buildings and roads was the primary cause of structural failure [10–12]. Although there have been several studies carried out about scour around structures, limited literature is available about tsunami-induced scour. Thus, post-tsunami field survey data are the primary source of information [13]. Based on the post-disaster field survey of the 2011 Tohoku tsunami, Jayaratne et al. [14] found that leeward toe scour is one of the primary failure mechanisms of coastal defence structures.

Knowing that the scour is one of the primary reasons for structural failure, studying the scour mechanism is of paramount importance in informing future design criteria. This can help in the development of robust design guidelines and mitigation measures [13].

There have been several studies in the past which investigated the scour around structures. Uda et al. [15] carried out laboratory experiments to study about scouring and collapsing mechanism of a revetment under the tsunami waves. The findings from the study indicated that the failure or collapse of the revetment was dependent on the topography of the reclaimed area and scour occurred around the toe during the tsunami downrush [16,17]. The effect of grain size on scour during tsunami run-up around a cylindrical structure was investigated using sand and gravel beds by [18]. The study concluded that when the sand was replaced with gravel, the area in which the scour occurred was reduced. However, this change did not always have an impact on the maximum scour depth.

Yoshii et al. [19] attempted to investigate the sedimentation and inundation caused by tsunami waves using super large wave flume at Central Research Institute of Electric Power Industry (CRIEPI), Japan. The study analysed the sediment transport and deposition in the shore areas or coastal hinterlands. They tried to explore the sediment movement around the structure under the influence of tsunami waves.

The adverse socio-economic and environmental impacts of this hydro-sedimentary process on coastal defence structures have made the researchers focus on the development of a numerical model to study the phenomenon. These studies have also led to the improvement of various numerical tools to better understand and predict complex sediment transport processes. Rapid advancement in computational capability in the last few decades has enabled the rapid development of numerical simulations.

Kim and Chen [20] integrated a computational fluid dynamics (CFD) model called FANS3D with a suspended sediment transport model to study complex flow problems. Two experimental programmes were first conducted to validate the new model (solver) and the sediment concentration results showed good agreement. The new solver was then extended to simulate sediment transport around the abutment in the channel bed and it showed well-simulated 3D suspended sediment transport results. Baykal et al. [21] employed a 3D hydrodynamic model, embedded with a $k-\omega$ turbulence model, sediment transport and morphological models, to investigate the effect of suspended load and vortex shedding on scour around a vertical circular cylinder subjected to steady current. The authors compared their numerical results against the experimental data and discovered that 50 % of the scour depth measured at the equilibrium stage is because of the suspended sediment transport and that the effects of vortex shedding at the beginning of the scour process are not pronounced.

Hongwei and Rodi [22] employed a 3D computer model to study the flow characteristics and sediment transport processes in the neighbouring parts of the dam of the Three Gorges hydroelectricity plant in the Yangtze River, China. The results of the free surface velocity and bed deformation resulting from the suspended load agree well with the laboratory measurements. Tofany et al. [23] developed a 2D RANS-VOF model to study the scour process in front of an impermeable vertical breakwater. They employed sediment transport formulae and bottom shear stress in the model to produce the scour patterns at the structure. An accurate near-bottom velocity and improved deposition patterns for coarse materials were reported.

Burkow and Griebel [24] investigated the scour patterns at a rectangular obstacle using the NaSt3D model and Exner's bed level equation to study fluid flow characteristics and sediment transport processes respectively. Both numerical and experimental results show good agreement. Zhang and Shi [25] studied the scour process of an underwater pipeline. They incorporated a bed-load sediment transport formula into the ANSYS Fluent modelling suite and simulated the bed deformation using dynamic mesh technology. There were good resemblances between the numerical and experimental results.

Commercial and open source computational fluid dynamics models have been employed to study scour processes around hydraulics structures. Ahmad et al. [26] and Sreedhara et al. [27] both employed REEF3D, a CFD model, to study the scour process around piers and piles respectively. Both studies concluded that numerical results matched well with the experiments. The FLOW-3D software was used by Li et al. [28] to simulate the hydrodynamics and local scour around a non-submerged spur dike. They reported 3 phases of the scour process; i.e. initial phase, the main scour phase and the balance phase, and testified that the first two phases are the most significant of the scour development process since most of the scour occurred during these stages.

Saponieri et al. [29] conducted a large-scale physical experiment at the new Delta flume (Delft, The Netherlands). They aimed to investigate the wave impact on a vertical wall placed in a dike and the morphological evaluation. They used the XBeach [30] model for their scour analysis. They compared the computed data with the experimental data and found out that the XBeach showed good reliability in the general evolution of the bed layer during the experiments. They concluded that this analysis allows to have a good prediction of general parameters of scour.

Kang et al. [31] studied the flow characteristics around a dike with varying ratios of length and depth. They did an experimental and numerical study of flow characteristics around a dike. They found out that when the length-to-depth ratio moves closer to one, three-dimensional flow patterns which can affect the scour, existed around the dike.

Tsunami-induced scour has long been a significant challenge in coastal engineering, as it can lead to the catastrophic failure of defence structures during extreme wave events. Various numerical and experimental studies have been conducted to investigate the underlying mechanisms of scour and develop predictive models [32] . However, a key novelty of this study lies in its focus on an underexplored aspect of tsunami-induced scour: the effect of coastal dike geometry on scour at the leeward side. While most prior studies generalise scour processes, this work specifically highlights the geometric influence on scour dynamics, offering new insights into the complex interactions between hydrodynamic forces and sediment transport.

Scour around coastal structures is a fundamental issue affecting both their design and stability. Tortumluoglu et al. [33] analysed equilibrium and temporal scour around the head of rubble mound breakwaters under both breaking and non-breaking wave conditions, showing that wave breaking considerably reduces equilibrium scour depth. Xu and Huang [34] examined wave-induced local scour around pile breakwaters and found that the maximum scour depth exhibits an exponential trend over time. In another experimental study, Yu et al. [35] investigated wave- and current-induced scour around anti-deposition permeable breakwaters using physical models.

It is well recognised that when waves directly impact a breakwater, the resulting scour in front of the structure generally occurs in a two-dimensional form [36]. Many earlier studies have also focused on two-dimensional scour processes [37–47]. For example, Sumer and Fredsøe [45] investigated two-dimensional scour at the trunk of rubble-mound breakwaters and proposed countermeasures for toe protection using both single and multiple layers of stones. Building upon the scour depth formula developed earlier by Sumer and Fredsøe [45], Myrhaug et al. [48] presented a method to estimate scour depth and determine the necessary width of the protection layer for the head of vertical-wall breakwaters and round-headed rubble-mound

breakwaters.

Despite the efforts of several numerical studies about the scour regime as discussed above, very few numerical studies consider the effect of coastal dike geometry on tsunami-induced scour at the leeward side. Thus, this paper will focus on the numerical investigation of the hydro-sedimentary dynamics at the leeward of a coastal dike. The study employed the tsunami-induced scour predictive model developed by Jayaratne et al. [14], which was based on comprehensive laboratory experiments. The model was rigorously validated using advanced numerical methods, including a hydrodynamic model and a sediment transport model.

Another novel contribution of this research is its integration of advanced numerical modelling approaches, such as the Reynolds-Averaged Navier-Stokes (RANS) equations for hydrodynamic simulations and turbulence-averaged Eulerian two-phase flow equations for sediment transport. These methods enable a highly detailed representation of both flow dynamics and sediment interactions, surpassing the capabilities of traditional modelling techniques.

The hydrodynamic model was formulated using the Reynolds-Averaged Navier-Stokes (RANS) equations, which are widely utilized to simulate turbulent flows by averaging the effects of turbulence over time. This approach allowed for a detailed representation of tsunami-induced flow dynamics. Additionally, the sediment transport model was developed based on the turbulence-averaged Eulerian two-phase flow equations, which account for the interactions between the fluid phase (water) and the solid phase (sediments). This method effectively captured the mobilization, transport, and deposition of sediments driven by tsunami-induced turbulent forces.

By bridging numerical and experimental approaches, this study provides a robust and reliable framework for predicting tsunami-induced scour, filling a critical gap in existing research. Moreover, the findings contribute to the development of more resilient coastal defence designs, particularly by incorporating the influence of dike geometry into scour prediction models. By integrating these numerical models with experimental data, the study established a robust framework for predicting scour under tsunami conditions, ensuring high reliability and accuracy in the assessment of sediment dynamics.

2. Experimental data used for numerical models

Jayaratne et al. [14] used the field data of the 2011 Tohoku tsunami, and laboratory experimental data to derive a practical scour depth predictive model at the leeward toe of a coastal dike. The field survey team measured the spatial extent of the scour, geometry of the collapsed or failed structures, digital photos and videos, coordinates of the survey locations and collected soil samples at damaged structures in Fukushima and Miyagi prefectures.

The laboratory experiments were conducted in a hydraulic flume of 8.6 m long, 0.305 m wide and 0.315 m deep at the University of East London (see Fig. 1). Three 1:50 scale non-porous coastal dike models with varying slopes and constant structure height of 0.1 m were used in the experiments (Fig. 2). Although small scale experiments are beneficial in many research studies, they can lead to inaccuracies due to scale effects, such as altered turbulence, sediment transport, and wave breaking dynamics. Increased viscous and surface tension forces may distort results, and sediment properties or boundary constraints might not scale realistically. Ensuring dynamic similarity and using hybrid turbulence modelling can mitigate these issues.

The impermeable beach slope in front of the structure was maintained at 1:10 throughout the study and the dam break method was employed to create a tsunami-like wave. The dam break gate was located 1 m from the start of the beach slope to allow full development of the wave.

The three model dikes had different seaward and landward slopes and crest widths to replicate the three damaged dikes in Ishinomaki (A), Iwate (B) and Soma (C) (Table 1). Further, these configurations were employed to study the hydrodynamic behaviour of the quasi-tsunami flow under several hydraulic variations.

A sand layer of 0.113 m was placed right after the landward of the model dike in order to measure the depths and extent of the scour profile. The average sand diameter (d_{50}) used to fill the landward region was kept at 0.35 mm.

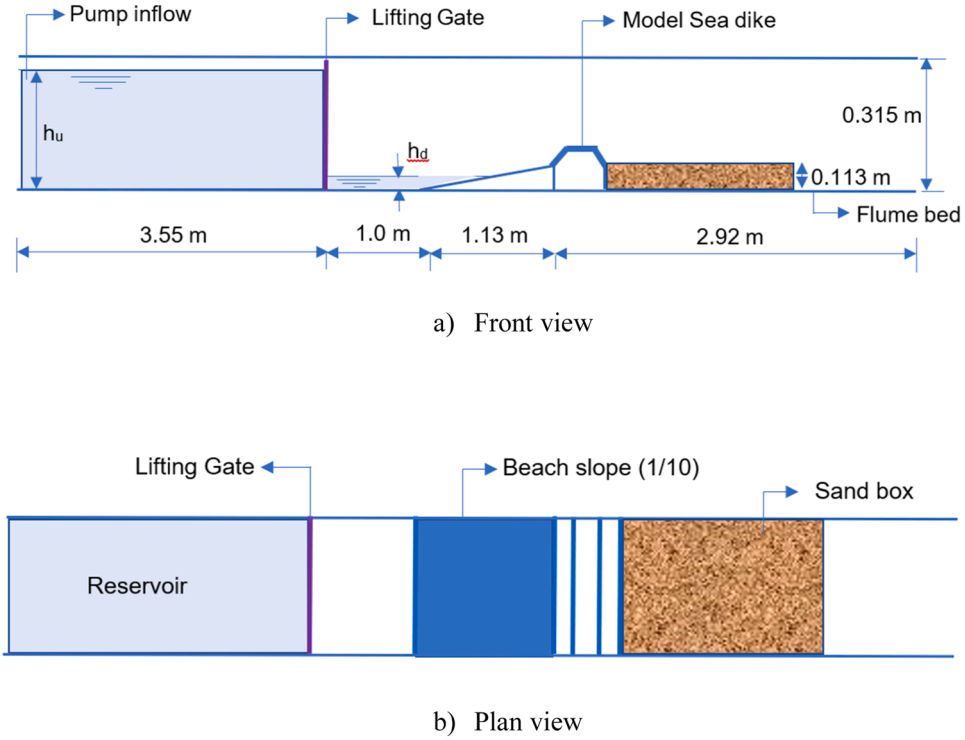

Fig. 1. Schematic experimental set-up of Jayaratne et al. [14] used in the present study.

a. Wave flume at University of East London

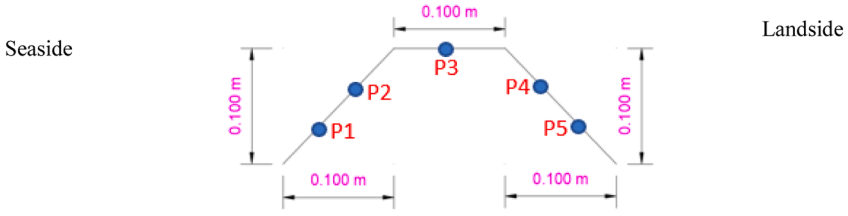

b. Model A

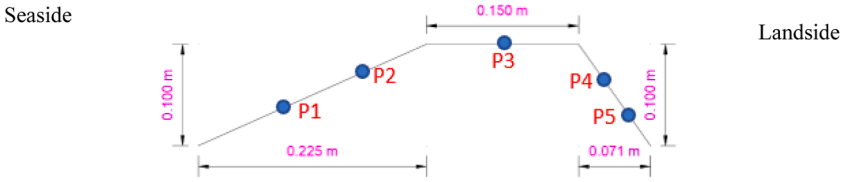

c. Model B

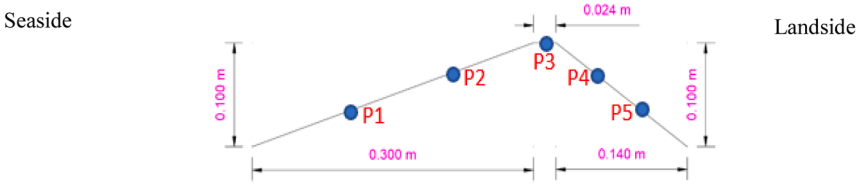

d. Model C

Fig. 2. a) Front view of hydraulic flume channel. b, c, d) Coastal dike model geometries tested in the present study, with pressure sensors P1-P5.

Table 1
Dimensions of the tested model dikes.

Dike geometry type	Crest width (cm)	Seaward slope	Landward slope
A	10	1: 1	1: 1
B	15	1: 2.25	1: 0.71
C	2.4	1: 3	1:1.4

Table 2
Tested hydraulic variations in the present study.

Hydraulic variation type	h_u (m)	h_d (m)	$\alpha_i \left(=\frac{h_d}{h_u}\right)$
I	0.3	0.015	0.050
II	0.3	0.030	0.100
III	0.3	0.050	0.167

The upstream water height behind the dam-break gate, h_u was maintained at 0.3 m throughout the study to ensure uniformity. The water depth downstream, h_d (seaward region of the dike) was varied to represent three distinct hydraulic conditions as specified in Table 2. These hydraulic conditions together with the geometry of the flume and the coastal dike models (Fig. 2) were represented and evaluated using a 2D numerical model.

The tsunami-like wave propagation after the dam was opened towards the dike and scour process were recorded by a video camera. The frame-by-frame video analysis of the fluid flow was used for further analysis including velocity detection. Five pressure sensors (MEAS France SO: FA59630. Model: EPX-N02–1B-/Z2/L1M/25 M. Serial number: Q1416Z. Range: 1 bar S. Measurement Specialties Inc.), P1-P5, digitised at a frequency of 25 kHz, were installed in 5 different locations in the model dikes (Fig. 2). Once the wave passes through the model

dikes and the scour process takes place, the scour depth in the leeward of the model dike were measured using a point gauge and video image analysis. The moving point gauge with a vernier scale was used to measure the size of the scour holes behind the model coastal dike, and a level was used to position a layer of sand during the scour process. The dynamic changes in scour depth and extent from the initial leveled plane-bed were recorded and analyzed using video imagery technique. It was estimated that the prototype scour duration is approximately 42 s.

3. Numerical investigation of wave propagation

The ANSYS Fluent (www.ansys.com/products/fluids/ansys-fluent), a CFD modelling suite, is used to simulate the 2D dam-break incompressible fluid flow. The realizable k-ε turbulence model was applied because of an accurate prediction of the mean-square vorticity fluctuation. This model has been proven to perform well in comparison to the other k-ε models used for separated and swirling flows [49,49,50]. However, some other models, such as the k-omega models, have also demonstrated the potential to simulate similar conditions effectively [51].

A major development on the standard k-ε model conducted by Shih et al. [52] as it presents a new formulation for the turbulent viscosity and the dissipation rate, ε, transport equation derived from a precise equation of the mean-square vorticity fluctuation.

Turbulent kinetic energy k,

$$\frac{\partial}{\partial t}(\rho k)+\frac{\partial}{\partial x_j}(\rho k u_j)=\frac{\partial}{\partial x_j}\left[\left(\mu+\frac{\mu_t}{6_k}\right)\frac{\partial k}{\partial x_j}\right]+p_k+p_b-\rho_\varepsilon-Y_M+S_k \quad (1)$$

Turbulent dissipation ε

$$\frac{\partial}{\partial t}(\rho\varepsilon)+\frac{\partial}{\partial x_j}(\rho\varepsilon u_j)=\frac{\partial}{\partial x_j}\left[\left(\mu+\frac{\mu_t}{6_\varepsilon}\right)\frac{\partial\varepsilon}{\partial x_j}\right]+\rho c_{1\varepsilon}S\varepsilon-\rho c_2\frac{\varepsilon^2}{k+\sqrt{\nu\varepsilon}}+c_{1\varepsilon}\frac{\varepsilon}{k}c_{3\varepsilon}P_b+S_\varepsilon \quad (2)$$

where, $c_1=\max\left[0.43,\ \frac{\eta}{\eta+5}\right]$, $\eta=S\frac{k}{\varepsilon}$, $S=\sqrt{2S_{ij}S_{ij}}$.

The model function c_1 is formulated as a simple function of η, which denotes the raio of the turbulence time scale to that of the mean strain. It allows c_1 to adjust dynamically to local flow conditions, thereby enhancing the capability of the model to simulate a diverse spectrum of turbulent flows. The modulus of the mean rate-of-strain tensor, S, plays a crucial role in characterising both the production and dissipation of turbulence, as it quantifies the overall rate of deformation within the flow field.

In these equations, P_k, P_b, and Y_M are calculated as shown in the standard k-ε model above. The term P_k signifies the production of turbulence kinetic energy arising from mean velocity gradients, providing a measure of the energy transferred from the mean flow to turbulent fluctuations as a result of velocity shear. P_b represents the generation of turbulence kinetic energy attributable to buoyancy effects. In addition, the parameter Y_M accounts for the influence of fluctuating dilatation in compressible turbulence on the total dissipation rate.

In these equations, P_k, P_b, and Y_M are calculated as shown in the standard k-ε model above. Turbulent eddy viscosity, $\mu_t=\rho c_\mu\frac{k^2}{\varepsilon}$, Where, $c_\mu=\frac{1}{A_0+A_s\frac{kU^*}{\varepsilon}}$,

$$U^*\equiv\sqrt{S_{ij}S_{ij}+\widetilde{\Omega}_{ij}\widetilde{\Omega}_{ij}},\ \widetilde{\Omega}_{ij}=\Omega_{ij}-2\varepsilon_{ijk}\omega_k,\Omega_{ij}=\overline{\Omega_{ij}}-\varepsilon_{ijk}\omega_k$$

$\overline{\Omega_{ij}}$ is the mean rate-of-rotation tensor observed in a rotating reference frame with angular velocity, ω_k. By default, - $2\varepsilon_{ijk}\omega_k$ is not included in FLUENT in the calculation of $\widetilde{\Omega}_{ij}$.

$$A_0=4.04, A_s=\sqrt{6}cos\phi$$

$$\phi=\frac{1}{3}cos^{-1}\left(\sqrt{6}\,W\right),\ W=\frac{S_{ij}S_{jk}S_{ki}}{\widetilde{S}^3},\ \widetilde{S}=\sqrt{S_{ij}S_{ij}},\ S_{ij}=\frac{1}{2}\left(\frac{\partial u_j}{\partial x_i}+\frac{\partial u_i}{\partial x_j}\right)$$

$$c_{1\varepsilon}=1.44, c_{2\varepsilon}=1.9,\ 6_\varepsilon=1.2,\ 6_k=1.0$$

Turbulent eddy viscosity, μ_t, is introduced as a modelled property to represent the augmented momentum transfer associated with turbulent eddies, which is not captured by molecular viscosity alone. Unlike the standard $k-\varepsilon$ model, in which the coefficient c_μ is assigned a constant value (typically $c_\mu=0.09$), the present approach defines c_μ as a function of local flow characteristics. This variable formulation of c_μ enables the model to more accurately capture turbulent flows exhibiting complex strain and rotational features.

For this study, the unstructured mesh was used around the beach slope and the coastal dike, while structured mesh was used in other regions of the studied domain. Due to the mesh size limitation of the product, the sizes varied between $\Delta x=\Delta y=$ 0.00001 m and 0.01 m with a minimum orthogonal quality of 0.97. Using orthogonality, the degree to which grid lines or surfaces are perpendicular to each other can be evaluated. In other words, orthogonal quality can be used to evaluate the quality of the mesh. The orthogonal quality for cells is computed using the face normal vector, the vector from the cell centroid of each adjacent cell, and the vector from the cell centroid to each of the faces. The effect of friction on the flow was not considered.

Fig. 3 depicts the different parts that were created to generate the boundary conditions required for the solution procedure. The parts created were: Left_Wall (Zone 1), Inlet (Zone 2), Free_Surface (Zone 3), Seaward_Slope (Zone 4), Crest (Zone 5), Landward_Slope (Zone 6), Right_Wall (Zone 7), Bottom_Wall (Zone 8), Back_Wall (Zone 9), Beach_Slope (Zone 10), and Left_Bottom_Wall (Zone 11). The designated zones denote specific areas within the computational domain that can be assigned tailored properties and boundary conditions. A coarser mesh size was applied to the offshore side of the flume, while the mesh resolution was refined to its highest level on the crest of the dyke and its backside. This finer resolution was essential to accurately simulate the overtopping flow and the scour area, specifically in regions 5, 6, and 7.

The tsunami-like waves were modeled using dam break flow (two-phase flow). The volume of fluid (VOF) with Piecewise Linear Interface Calculation (PLIC), a method developed by Youngs [53] was used to model the interface between air and water. Additionally, Courant number was estimated using the following equation.

$$C=\frac{U\Delta t}{\Delta h} \quad (3)$$

where U is velocity of flow, Δt is time step, and Δh is the mesh size. Throughout the simulation sections and models, the mesh size and time step was kept as 0.01 m and 0.001 s respectively. To determine the ratio between the distance a fluid particle travels in a single time step and the spatial grid spacing, Courant numbers were calculated based on the velocity distributions described by Abimbola [54]. The results are presented in Table 3.

To overcome the large computational time requirement for a very fine grid close to the near-wall regime, the scalable wall function was used. This function treats challenging effects such as viscous effects that can be found in turbulent flows like tsunamis, by dynamically adjusting to mesh resolution and viscous effects, ensuring accurate and stable simulations of high Reynolds number flows. This wall function consists of a logarithmic law together with a limiter in the dimensionless distance from the wall of the standard wall function developed [55]. An initialisation of a hybrid solution is applied to speed up the convergence of the numerical simulations. The hybrid solution is an initialization method that blends the standard initialisation and patch initialisation techniques. It calculates flow field variables such as pressure, velocity, and temperature using simplified approximations such as Laplace's equation, offering a more physically realistic starting point for complex

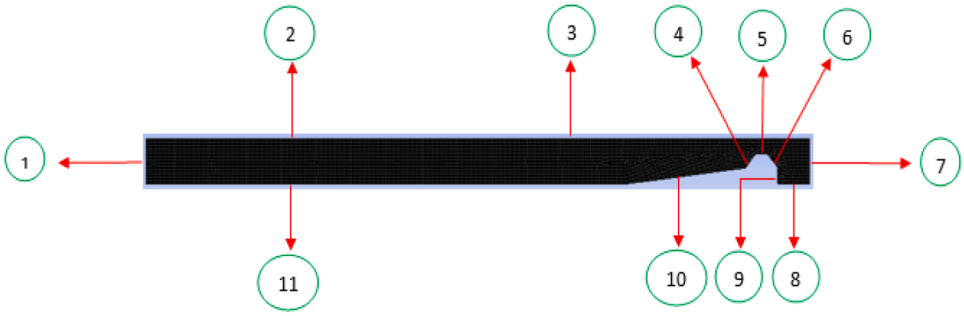

Fig. 3. Different model sections set up in ANSYS Fluent Software [(1) Left wall; (2) Inlet [the upstream section of the gate]; (3) Free surface [the downstream section of the gate]; (4) Seaward slope; (5) Crest; (6) Landward slope; (7) Right wall; (8) Bottom wall; (9) Back wall; (10) Beach slope; and (11) Bottom left wall].

Table 3
Estimated Courant numbers based on different flow conditions.

Model	Time step	Mesh size	Lowest flow velocity	Highest flow velocity	Lowest Courant number	Highest Courant number
A	0.001	0.01	1.79	1.87	0.179	0.187
B	0.001	0.01	2.25	2.62	0.225	0.262
C	0.001	0.01	1.79	1.85	0.179	0.185

simulations. The Δt was set at 0.001 s the estimated maximum iterations/time step was found to be 20. This led to 6000-time steps of the flow. Fig. 4 presents the distributions of air and water volume fractions, which were employed to represent the interface between the two phases during and after the tsunami-like wave overtopping event over one of the model dikes, Model A.

3.1. Total wave pressure (TWP)

Tsunami wave pressure consists of two components: hydrostatic and dynamic pressure. Arimitsu [56] explained the effect these two components of tsunami waves can have on a coastal structure. Moreover, Arimitsu [56] opined that when the main body of a tsunami impacts a structure, a considerable amount of hydrostatic pressure and the least amount of dynamic pressure are generated, on the other hand when the bore of the wave impacts a structure, the least amount of hydrostatic pressure and a significant amount of large dynamic pressure are generated. The total wave pressure (TWP) values from the numerical simulations are discussed in the following sub-sections.

ANSYS Fluent was used to derive pressure values at points corresponding to the actual pressure sensors used in the laboratory experiments. The simulations maintained the same dike geometry and hydraulic conditions exactly as those used in the laboratory experiments. Total Wave Pressure (TWP) values for all three tested dike models A, B, and C were obtained under three different hydraulic conditions as described in Table 1. From the simulation data, the maximum pressure (P_{max}) recorded by all five pressure sensors and the total duration of the tsunami flow (t_d) were extracted subsequently, pressure values against time series were plotted, normalising by dividing them by P_{max} and t_d.

3.1.1. Dike model A

The P/P_{max} against t/t_d values for the three hydraulic conditions used in dike model A is depicted in Fig. 5. A sharp spike in the pressure values was observed for all five sensors. This might be caused by the sudden impact of the wave on the model dike. Pressure at points P1 and P2, in the seaward slope of the dike were observed to be the highest under all three tested hydraulic conditions. This is plausible as the wave hits the seaward-facing side with maximum energy. A drop in P/P_{max} as time increases due to a drop in TWP is observed for all the sensors. It was observed that the sensors P4 and P5 had a gradual increase and decrease compared to the sensors P1 and P2. This suggests a more subdued and delayed response to water flow, which could be due to the dike absorbing the impact from the seaward side and only a portion of the energy reaching the landward side. From the plots we can comfortably conclude that the given dike geometry (dike model A) significantly reduces the pressure from the seaward side (P1) to the landward side (P5) for all tested hydraulic conditions, which demonstrates its effectiveness in protecting the landward area.

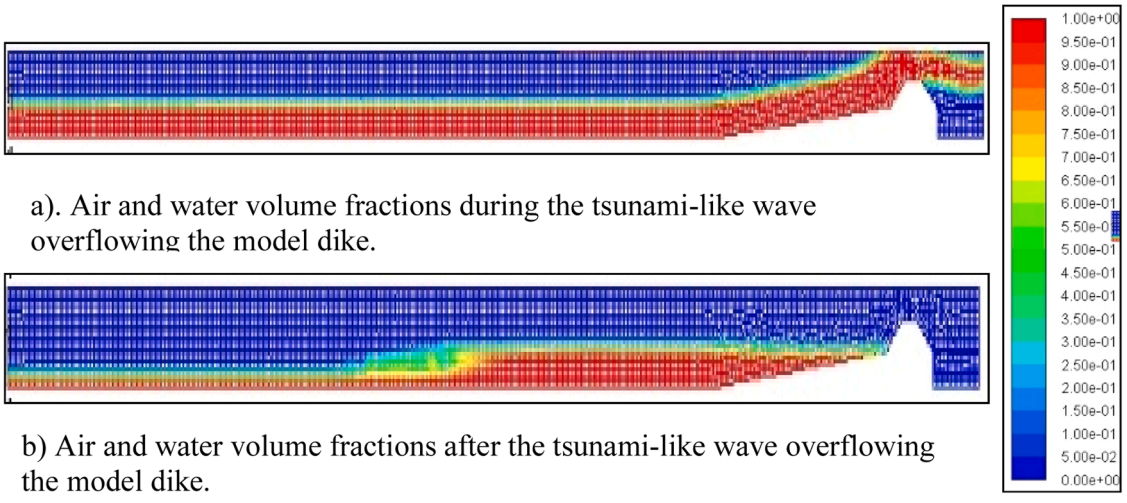

Fig. 4. Air-water interface during and after the tsunami-like wave overtopping event of the model dike A.

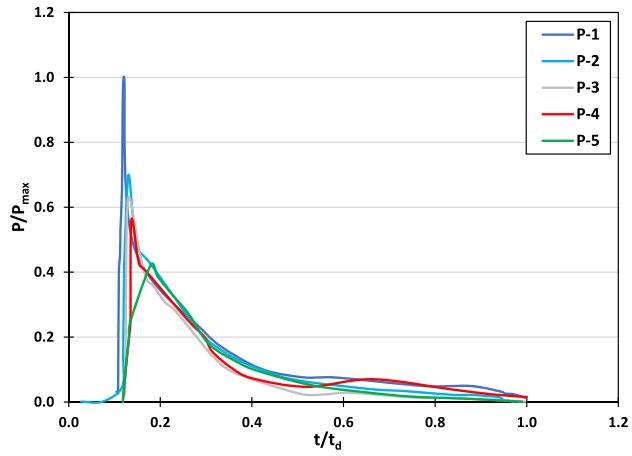

a. Type I hydraulic condition

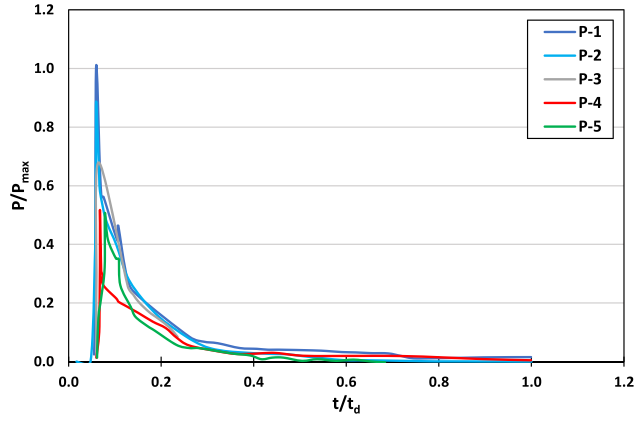

b. Type II hydraulic condition

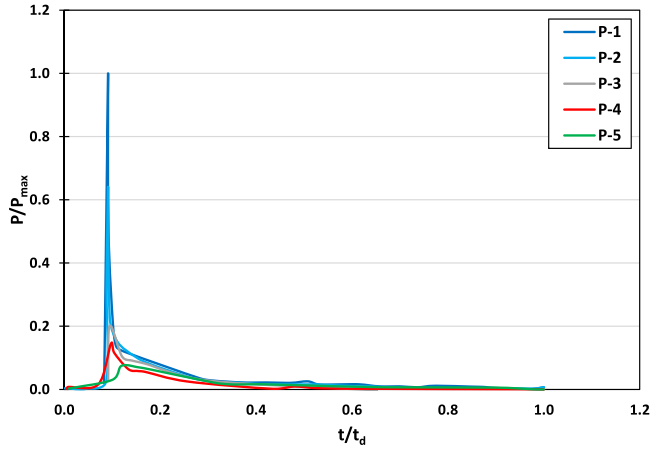

c. Type III hydraulic condition

Fig. 5. Numerical results from ANSYS Fluent model. Total wave pressure distribution in Model A under three hydraulic conditions. Different types of hydraulic conditions are given in Table 2.

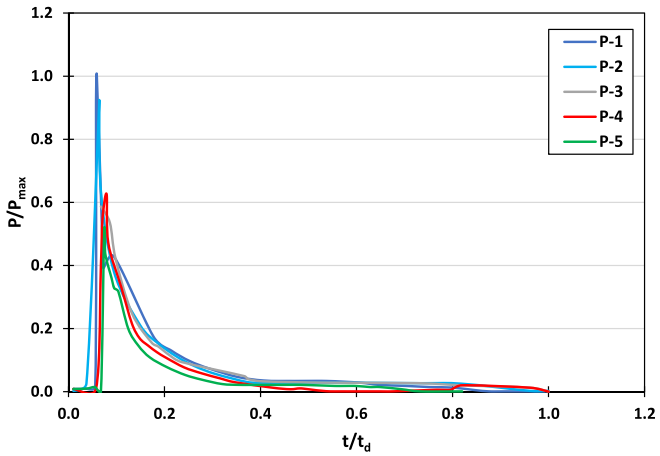

a. Type I hydraulic condition

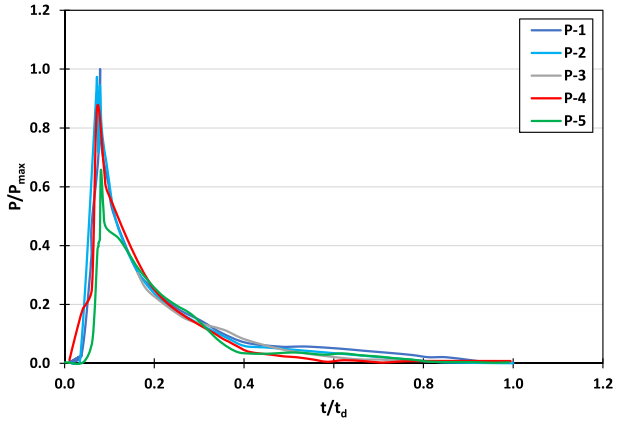

b. Type II hydraulic condition

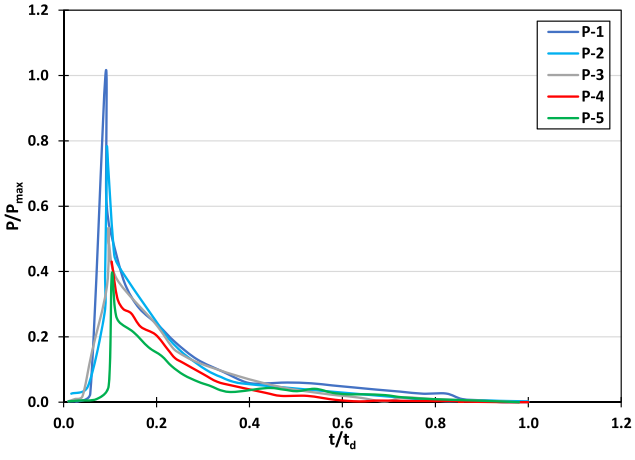

c. Type III hydraulic condition

Fig. 6. Numerical results from ANSYS Fluent model. Total wave pressure distribution in Model B under three hydraulic conditions. Different types of hydraulic conditions are given in Table 2.

3.1.2. Dike model B

The P/P_{max} against t/t_d values for the three hydraulic conditions used in dike model B are depicted in Fig. 6. A sharp spike in the pressure values was observed for all five sensors. However, it can be observed that the pressure values in P1 and P2 are similar in contrast to model A. Similarly, the same pattern was observed at P4 and P5. From Table 4, the pressure values at P3 were observed to be very similar to both model dikes and all tested hydraulic conditions. Steeper slopes (model A) may result in the wave impingement closer to the dike and thereby have more energy concentrated around the dike. This results in more impact energy and therefore high peak values as seen in Fig. 5 and Table 4. Moreover, reflected waves in steeper slopes play a crucial role in reducing the

Table 4
Experimental (Exp.) and numerical (Num.)TWP obtained at P1-P5.

Pressure sensor	Downstream depth (h_d) / m								
	0.015			0.03			0.05		
	Maximum pressure / bar								
	Exp.	Num.	Exp./Num. ratio	Exp.	Num.	Exp./Num. ratio	Exp.	Num.	Exp./Num. ratio
Model A									
P1	0.5	0.43	1.16	0.32	0.28	1.14	0.32	0.64	0.50
P2	0.38	0.28	1.36	0.35	0.25	1.4	0.53	0.43	1.23
P3	0.35	0.17	2.06	0.35	0.18	1.94	0.41	0.13	3.15
P4	0.3	0.15	2.00	0.39	0.18	2.17	0.34	0.1	3.40
P5	0.41	0.14	2.93	0.35	0.17	2.06	0.41	0.08	5.13
Model B									
P1	0.49	0.33	1.48	0.38	0.2	1.90	0.43	0.23	1.87
P2	0.41	0.32	1.28	0.4	0.21	1.90	0.38	0.18	2.11
P3	0.36	0.19	1.89	0.36	0.18	2.00	0.37	0.12	3.08
P4	0.41	0.18	2.28	0.36	0.18	2.00	0.36	0.09	4.00
P5	0.45	0.17	2.65	0.4	0.17	2.35	0.39	0.09	4.33
Model C									
P1	0.6	0.34	1.76	0.35	0.27	1.30	0.35	0.19	1.84
P2	0.37	0.28	1.32	0.36	0.21	1.71	0.36	0.16	2.25
P3	0.38	0.21	1.81	0.4	0.17	2.35	0.38	0.13	2.92
P4	0.4	0.2	2.00	0.33	0.17	1.94	0.33	0.12	2.75
P5	0.48	0.18	2.67	0.44	0.17	2.59	0.33	0.11	3.00

overall pressure values. A gentle seaward slope of the dike allows waves to propagate over a longer distance as they approach the dike crest. This process takes place smoothly. This is evident from Fig. 6 that the pressure drops are smooth and less abrupt. As the reflected waves play less role in gentle curves, the pressure drops may not be significant.

This is evident from the pressure values in Table 4, where pressure drops under all three tested hydraulic conditions were 66 % in Model A, compared to 41 % in Model B.

3.1.3. Dike model C

Fig. 7 indicates a similar pattern to model C, with the highest pressure at P1 and decreasing towards P5. Dike model C had a sharp crest, which might have allowed more overtopping, which could result in a more even distribution of pressure along the dike length. This could be why the pressures at P3, P4 and P5 did not drop sharply and remained consistent over time.

Under hydraulic condition 1, the pressure drops recorded by sensors P1–P5 were 18 % in Model A, 8 % in Model B, and 20 % in Model C. In contrast, under hydraulic condition 2, pressure increases were observed, 9 % in Model A, 5 % in Model B, and 26 % in Model C. Under hydraulic condition 3, pressure in Model A increased by 28 %, while Models B and C showed pressure drops of 9 % and 6 %, respectively.

The numerical data in Table 4 demonstrate that dike model B exhibited the lowest peak pressure at measurement point P1 in the numerical study. The gentler slopes of model C, compared to models B and A, induced a gradual decay in wave pressure. Conversely, the steeper slopes of model A resulted in the largest change in the TWP across the three hydraulic variations, with differences of 0.29 bar, 0.11 bar, and 0.56 bar. A consistent reduction in exerted pressure was observed across all tested geometries, attributable to energy dissipation in tsunami waves as they propagate landward. This phenomenon arises from increased shear forces in the downstream water depths, which diminish wave energy and consequently reduce hydraulic pressure on the dike structures.

Analysis of pressure sensor data P1–P3 for all the models revealed that 74 % of initial impact wave measurements exhibited experimental-to-numerical pressure ratios ≤ 2. This agreement diminished to 53 % when incorporating all five sensor datasets, indicating limitations in the capacity of the Reynolds-averaged Navier–Stokes (RANS) model to resolve secondary wave dynamics. While the 2D turbulence model successfully captured primary wave behaviour in the dam-break flume, turbulent interactions of the upstream flow with the downstream water, beach slope morphology, and seaside dike geometry were inadequately represented.

The observed variability in pressure data obtained from both experimental and numerical investigations highlights the need to verify the validity of the computational framework and the simulated pressure results. This is achieved by comparing the numerical outputs with experimental measurements of dam-break flows over a dry horizontal bed, as reported by Lobovsky et al. [57].

The numerical model replicated the experimental configuration within a small open channel of dimensions 1.61 $m \times 0.6\ m \times 0.15$ m, incorporating a water column height of $H = 300$ mm behind the dam gate. Pressure sensors 1–4, positioned at locations consistent with the laboratory setup, acquired data at a sampling frequency of 20 kHz. The locations of the sensors are as follows: P1 was positioned 3 mm, P2 at 15 mm, P3 at 30 mm, and P4 at 80 mm above the base of the flume, with all sensors aligned at the mid-section of the impact wall.

The pressure sensor 4, situated at the uppermost position, recorded the maximum dynamic pressure attributable to direct flow impact, whereas sensor 1, at the lowest elevation, registered the minimum peak pressure. This outcome contrasts with experimental observations, wherein sensor 1 exhibited the highest pressure peak and sensor 4 the lowest, as depicted in Table 5. Despite this inversion, the simulated peak pressure range aligned closely with experimental values; within 10.07 % of each other. The inverse relationship stem from divergent flow propagation dynamics. Experimental results indicated a downward-inclined free surface profile in the direction of the flow, while simulations produced an upward inclination (Fig. 8). Specifically, the downward slope of the free surface in the experimental study results in the secondary wave collapsing onto sensor 4, whereas the upward slope observed in the numerical simulation causes the secondary wave to impact sensor 1. Hu, Zhang, and Li [58] reports investigations in which two-dimensional numerical solvers were unable to accurately capture the free surface in the near-field region, although their accuracy improves as the flow advances downstream. To address this limitation in the context of this small-scale channel, the peak pressure range and the percentage difference in the range of peak pressures have been utilised, thereby maintaining accuracy of the numerical setup. Notably, turbulence effects arising from secondary waves were inadequately captured by the 2D turbulence model (Fig. 9).

RANS models are widely favoured in engineering and industrial applications due to their lower computational demands compared to LES (Large Eddy Simulation) and DNS (Direct Numerical Simulation). While

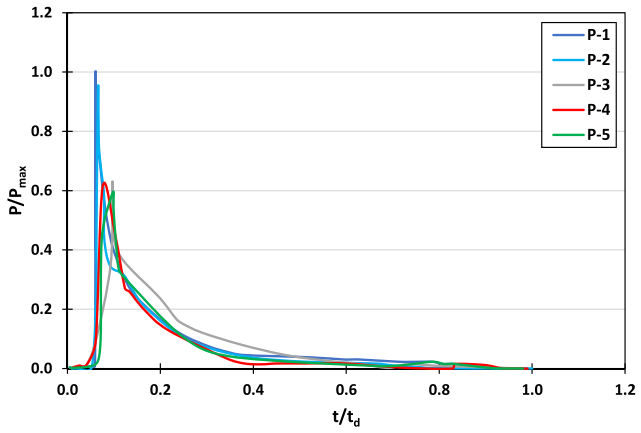

a. Type I hydraulic condition

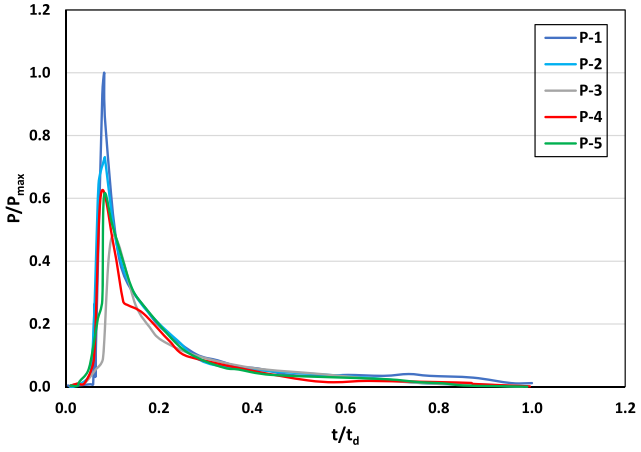

b. Type II hydraulic condition

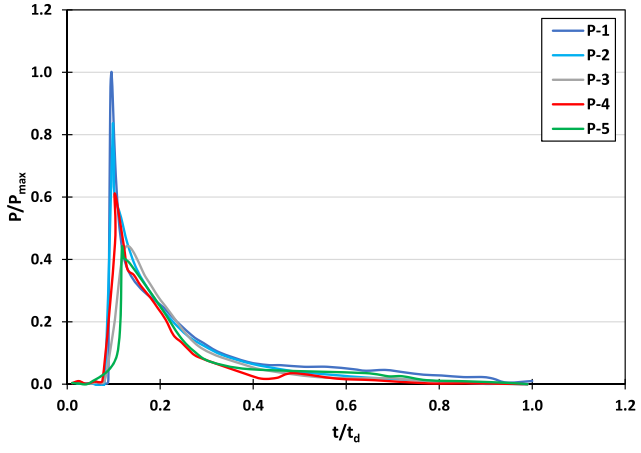

c. Type III hydraulic condition

Fig. 7. Numerical results from ANSYS Fluent model. Total wave pressure distribution in Model C under three hydraulic conditions. Different types of hydraulic conditions are given in Table 2.

RANS relies on modelling all turbulent motions, which makes it less accurate than the other methods, it is robust, straightforward to implement, and suitable for a broad range of engineering practical problems. In contrast, LES and DNS provide more detailed and accurate representations of turbulent flows but require significantly more computational resources, making them less practical for routine use. The observed discrepancies align with recognised constraints of 2D turbulence modelling, including pressure gradient inaccuracies and challenges in resolving laminar–turbulent transitional regimes. Furthermore, three-dimensional flow effects, particularly eddy structures arising from hydraulic structure interactions, were insufficiently characterised. These findings underscore the need for advanced computational approaches to partially resolve turbulent eddies and improve predictive fidelity in complex hydraulic scenarios.

Table 5
The peak pressure comparison between Lobovsky et al. [57] experimental study and the numerical study, for $H = 300$ mm.

Study type	Experimental study Lobovsky et al. [57]	Numerical study
Pressure sensor	Peak Pressure (bar)	Peak Pressure (bar)
Sensor 1	0.014	0.089
Sensor 2	0.035	0.057
Sensor 3	0.076	0.045
Sensor 4	0.086	0.023
Peak pressure range	0.073	0.066
Percentage difference in peak pressure range	10.07 %	

3.2. Overflowing wave pressure

When the bore impacts on the back of a model dike (landward slope of the dike), an overflowing wave pressure is generated. Mizutani and Imamura [59] established that its maximum value P_{om} has a relationship with the maximum flow velocity over the crest close to the landward region V_m, the water density ρ, the landward slope angle θ_2, gravitational acceleration g, and dike height measured at the leeside H_{d2}, as expressed in Eq. (4).

$$\frac{P_{om}}{\rho g H_{d2}} = 2\sqrt{2}\,\frac{V_m \sin\theta_2}{\sqrt{g H_{d2}}} \tag{4}$$

The average error, E, expressed mathematically in Eq. (5) shows the applicability of the simulated results against the measurements.

$$E = \frac{\sqrt{\sum_{i=1}^{N}(\widehat{Y} - Y_i)^2}}{N} \tag{5}$$

where, $\widehat{Y}$ is the model data, Y_i is the measured data and N is the total number of data used.

To compare the results obtained from the experimental study and numerical study, they were verified against the mathematical formula developed by Mizutani and Imamura [59], which is depicted in Fig. 10.

Fig. 10 demonstrates that models B and C exhibit closer alignment with the overflowing wave equation proposed by Mizutani and Imamura [59] compared to model A. It was observed that the numerical values diverge from experimental results. The observed discrepancies between experimental and numerical overflowing wave pressures are likely attributable to the turbulent interactions between the primary dam-break wave and the beach slope. The two-dimensional modelling approach may have either overlooked or excessively simplified the complex flow structures present in the system. To accurately resolve the turbulence, eddy formation, and vortex dynamics phenomena, it is necessary to employ a range of three-dimensional turbulence models capable of capturing the intricate flow features inherent to these hydraulic scenarios.

Table 6 presents the normalised pressure datasets derived from both the experimental investigation and the numerical analysis. The corresponding error values for the experimental and numerical data are also provided. It indicates that the numerical results for coastal dike models B and C exhibit reduced deviation from both the maximum overflowing

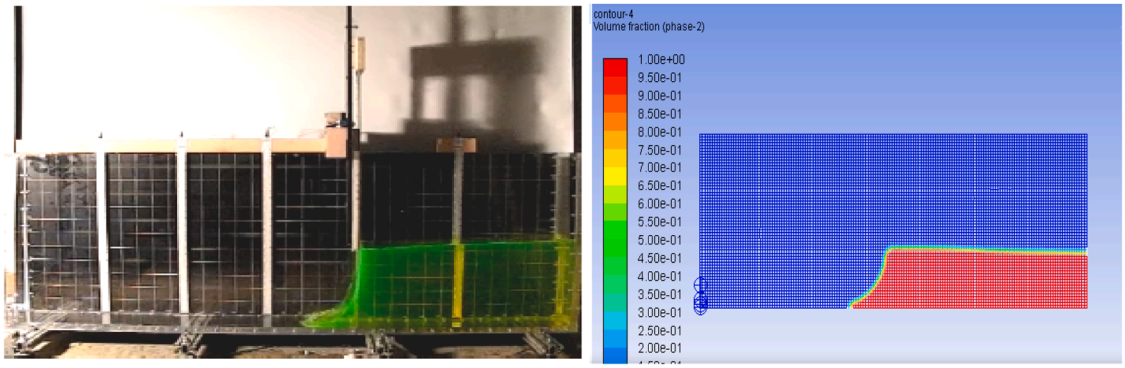

Fig. 8. Free surface profile and upstream wave at the instant of complete dam gate removal. $H = 300$ mm, experimental study by Lobovsky et al. [57] (left), numerical study (right).

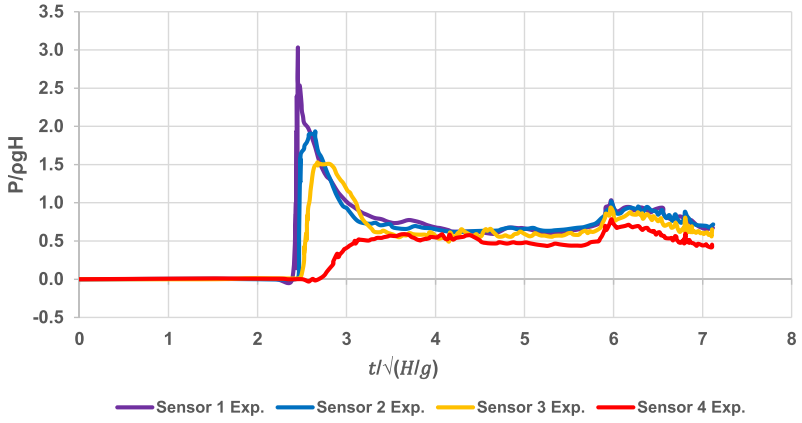

a) H = 300 mm; typical impact event pressure signals from four pressure sensors, experimental study by Lobovsky et al. (2014).

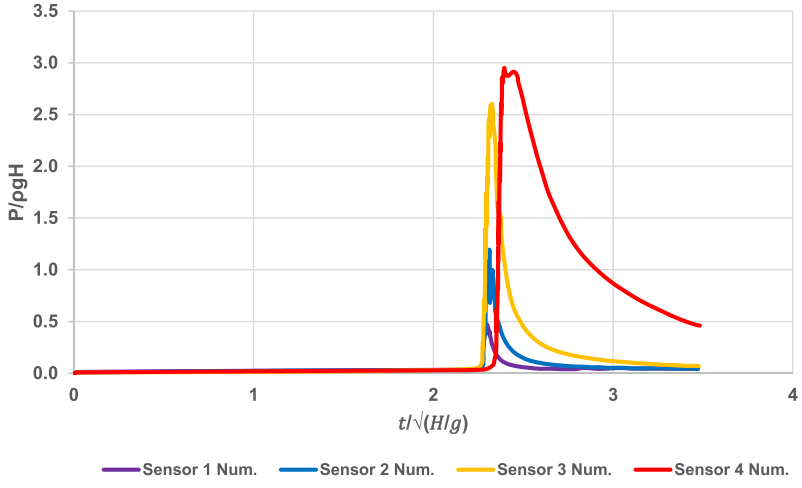

b) H = 300 mm; impact event pressure signals from four pressure sensors, numerical study.

Fig. 9. Comparison of impact event pressure signals from four pressure sensors during experimental and numerical studies for $H = 300$ mm.

pressure equation and the laboratory data reported by Jayaratne et al. [14]. The numerical model data of model A has the largest deviation from both Eq. (4) and laboratory measurements. The variations could be attributed to the different scales at which the studies were conducted.

Further, this also may be because of the limitation of the numerical model in which the tests were conducted. The events in the experimental study were digitised at a frequency of 25 kHz while the numerical work based on RANS modelling is digitised at 1 kHz. This method of time-averaged continuity and Navier-Stokes equations is not sufficient to fully describe the processes at all length scales. It makes it difficult to accurately capture the flow unsteadiness and the dynamics of small scales. About 19 trillion cells would be required to fully study this open channel flow problem in the 3D domain with a Reynolds number of approximately 8×10^5. Thus, we can understand the difference in the

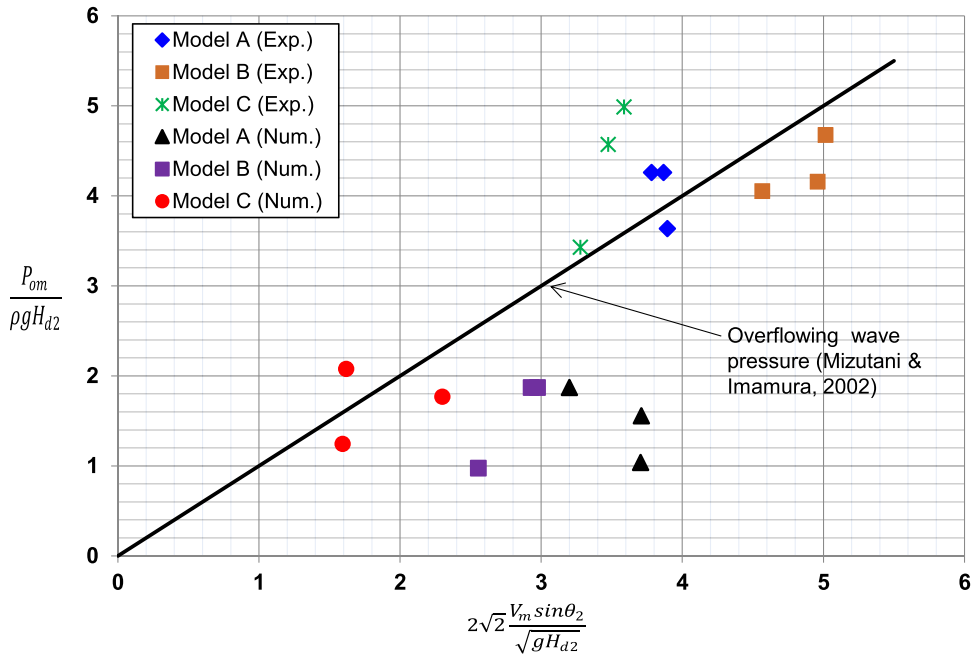

Fig. 10. The relationship between overflowing wave pressure and flow properties from experimental (Exp.) and numerical (Num.) simulations.

Table 6
Comparison of averaged error of experimental and numerical values of overflowing wave pressure.

Dike geometry type	$X = 2\sqrt{2}\frac{V_m sin\theta_2}{\sqrt{gH_{d2}}}$ Calculated using data from the numerical study	$Y_i = \frac{P_{om}}{\rho g H_{d2}}$ Calculated using data from the numerical study	$\hat{Y} = \frac{P_{om}}{\rho g H_{d2}}$ Calculated data using the overflowing wave pressure model (Eq. (4))	The average error, E, of the numerical data, where $N = 3$ for each of the three model dike sets	The average error, E, of the experimental data of Jayaratne et al. [14], where $N = 3$ for each of the three model dike sets
	3.71	1.56	3.71		
A	3.21	1.87	3.21	1.22	0.18
	3.71	1.04	3.71		
	2.93	1.87	2.93		
B	2.97	1.87	2.97	0.55	0.46
	1.62	0.98	1.62		
	1.62	2.08	1.62		
C	2.30	1.77	2.30	0.26	0.56
	1.59	1.25	1.59		

values obtained by experimental and numerical studies.

4. Numerical scheme for the hydro-sedimentary process

The hydro-sedimentary dynamics of the landward side of the structure are studied by using the open-source code-named "SedFoam 2.0" developed by Chauchat et al. [60]. The sediment stress was modelled using the kinetic theory of granular flows, and the k-ε turbulence model was employed to simulate the turbulent flow regimes. The flow velocities that induced the scour was determined by incorporating the shear stress values from the hydrodynamic study into the logarithmic velocity distribution. These velocities were incorporated through a logarithmic velocity distribution to ensure consistency with the hydrodynamic boundary conditions. The use of a logarithmic velocity profile is particularly significant in coastal engineering as it accurately represents the vertical distribution of flow velocities in turbulent boundary layers, such as those occurring near the seabed. This approach ensures a realistic coupling between the hydrodynamic model (ANSYS) and the sediment transport model (SedFoam), enhancing the reliability of sediment transport predictions under complex flow conditions. An overview of the theory behind the SedFoam 2.0 is depicted in Fig. 11.

4.1. Logarithmic velocity distribution

The Von kármán's logarithmic velocity distribution states that the average inlet velocity at a certain point is related to the distance from that point to the solid boundary. Keulegan [61] showed this relationship in Eq. (6).

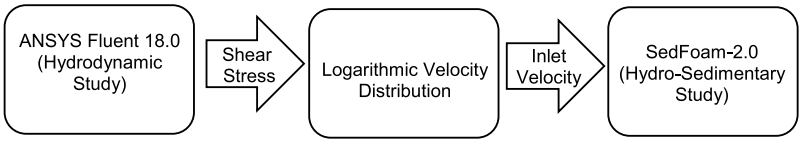

Fig. 11. Integration of different CFD modelling tools for the investigation of the hydro-sedimentary dynamics at dikes.

$$\frac{u}{u_*} = \frac{1}{k} ln\left(\frac{z}{z_o}\right) \tag{6}$$

where u is the inlet velocity, $u_*(= \sqrt{\frac{\tau_w}{\rho}})$ is the shear velocity, z is the perpendicular distance from the solid boundary, z_o is an integration constant, k is the Von kármán's constant.

For hydraulically rough flow, $z_o = 2.5\ d_{50}/30$, where d_{50} is the median diameter of the sediment. This changes the inlet velocity to that shown in Eq. (7).

$$u(z) = \frac{1}{k}\sqrt{\frac{\tau_w}{\rho}} \ln\left(\frac{30z}{2.5d_{50}}\right) \tag{7}$$

where, τ_w is the solid boundary shear stress, and ρ is the density of water.

4.2. Shear stress at bottom wall

The mean shear stress τ_w at the bottom solid boundary (see Fig. 3, Bottom boundary after the model dike) in the landward of the three model geometries was processed after the hydrodynamic study of the wave in ANSYS Fluent 18.0 software.

The time-averaged shear stress values computed through numerical analysis for all three tested model dike models and for all three hydraulic conditions are given in Table 7.

It can be noted from Table 7 that, all the mean shear stresses of the three models first increased during the Type II hydraulic test conditions before they finally decreased during the Type III hydraulic test condition. The influence of downstream water depth on the upstream water depth is reflected in the resulting average shear stress values. When the dimensionless initial downstream water depth, α_i, exceeds 0.100 under hydraulic variation II, the frictional resistance associated with the downstream water depth becomes significant, leading to a reduction in the average shear stress. A comparable pattern, characterised by a general reduction in bore velocity with increasing downstream water depth, was observed in the experimental data reported by Abimbola [54].

The bottom shear stress on the landward side of the model dike provides an indication of the hydro-sedimentary processes occurring within this region.

4.3. Model setup, mesh generation and initial boundary conditions

Fig. 12 provides a focused view of the landward region previously identified in Fig. 3. In the numerical model, a sand bed measuring 0.3 m in length with density, $\rho_a = 1602\ kg/m^{-3}$, mean particle diameter $d = 0.00035$ m, and shape factor = 0.5 was modelled. The density of water $\rho_b = 1000\ kg/m^3$ and kinematic viscosity $\nu_b = 1 \times 10^{-6}\ m^2s^{-1}$ were set. The flow depth h_o and the initial bed level h_b are 0.202 m and 0.113 m respectively replicating the experimental set-up.

Table 7
Time-average shear stress values at the bottom boundary (zone 2 in Fig. 12) for three different model geometries under three hydraulic variations.

Dike geometry type	Hydraulic condition type	Average shear stress (Pa)	ΔTWP = P1 – P5 [Total wave pressure difference between the seaward and landward slope of a dike]
	I	2.52	0.29
A	II	2.92	0.11
	III	2.88	0.56
	I	4.21	0.16
B	II	6.23	0.03
	III	4.65	0.14
	I	2.88	0.16
C	II	3.48	0.10
	III	2.67	0.08

An initial coarse mesh comprising 31,200 cells was established with spatial resolutions of Δx = 0.00125 m and Δz = 0.305 m applied uniformly to both water and sediment phases. Distinct Δy values of 0.0014125 m (sediment region) and 0.00404 m (water region) were implemented. This configuration proved unstable during scour process simulation, resulting in premature termination at $t = 0.5$ s. Subsequent iterative grid refinement was conducted until a stable fine mesh resolution was achieved, enabling robust temporal evolution of the system. Eight hundred thousand grid cells with $\Delta x = 0.000375$ m and $\Delta z = 0.305$ m in both water and sediment regimes were included to replicate the model area, while $\Delta y = 0.000226$ m and 0.000404 m in the sediment and water regions respectively were set. The time step size of 0.001 s and maximum iterations per time steps of 20 were estimated by trial and error.

With reference to Fig. 12, zones (2) and (4) were set as wall boundaries, zone 3 was set as the inlet boundary, zone 1 was set as the symmetry plane, and zones 5 and 6 were set as outlet boundary conditions. The velocity of both water and sediment phases, the sediment concentration (α – solid phase), the turbulence kinetic energy (TKE) and the TKE dissipation variables (ε or ω) are set based on 1D simulation results using funkySetFields. The details of the boundary conditions are summarised in Table 8.

4.4. Scour profile characteristics

ParaView-4.1.0 (www.paraview.org) was used to visualise the sediment concentration results. The morphological changes of the sediment beds in the landward region, obtained using SedFoam 2.0 were presented in Fig. 13. Scour profiles for each testing condition were plotted on a normalised graph where D_s is the scour depth, h_b is the initial bed level, h_l is the horizontal length of the sandbox and L_s is the corresponding length at each scour depth.

All three dike models as depicted in Fig. 13, exhibit the most pronounced scouring at hydraulic condition II. Model B, characterised by the highest average shear stress, the broadest crest width, and the steepest landward slope, demonstrates a distinct scour profile in the downstream region compared to models A and C. The location of its maximum scour depth is the furthest away from the landward toe. An increase in shear stress is directly associated with the initiation and progression of scour depth, as it reflects an enhanced erosive force acting upon the sediment bed. Duan et al. [62] interpret that the presence of dikes enhances both shear stress and turbulence intensity at the riverbed by concentrating the flow, thereby initiating local scour processes in the vicinity of the dikes. Hou et al. [63] elucidated the fundamental mechanism by which a submerged water jet induces the formation of a scour hole. This process arises from the momentum exchange between the sediment and the ambient fluid environment, occurring when the boundary shear stress imparted by the jet exceeds the shear strength of the cohesive sediment.

For Model A, the maximum scour depth measurement of 0.018 m was recorded for hydraulic condition I. This value increased to 0.021 m and slightly reduced to 0.0205 m when the hydraulic condition changed from II and III. For the case of Model B, hydraulic condition I, II and III gave 0.029 m, 0.041 m and 0.031 m maximum scour depths respectively. Hydraulic condition I generated a maximum scour depth of 0.0205 m for Model C. For the same model, this value increased to 0.024 m and then decreased to 0.0196 when the hydraulic condition changed from II to III. The rise-and-fall scour depth result pattern is similar to the pattern observed in the average shear stress values presented in Table 7.

Fig. 14 gives a comparison between the time-averaged shear stress and maximum scour depth derived from SedFoam 2.0 software. It can be observed that, when the shear value increases, the scour also increases. It is understandable that when the shear force near surface increases, it initiates sediment transport thus resulting in scour. The analysis demonstrates a direct correlation between the average shear stress, the maximum scour depth, and its corresponding horizontal position along

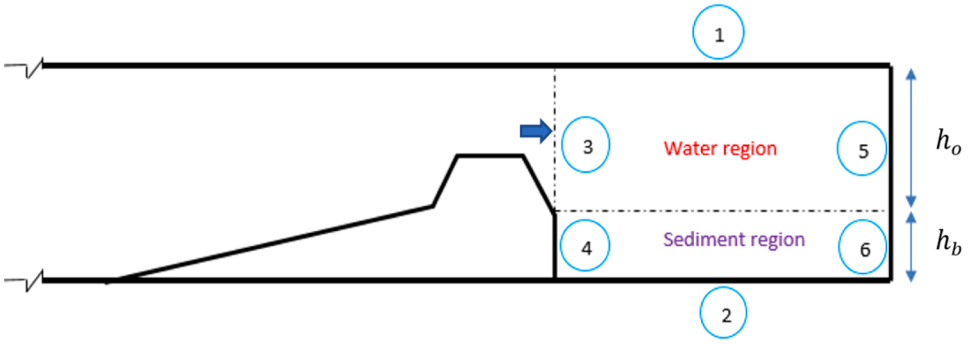

Fig. 12. Schematic sketch of various sections of landward region [(1) Top boundary; (2) Bottom boundary; (3) Inlet water boundary; (4) Inlet sediment boundary; (5) Outflow water boundary; (6) Outlet sediment boundary].

Table 8
Summary of boundary condition in the 2D sediment scour experimental configuration: zG = zeroGradient, fV = fixedValue, dM = directionMixed, fFP = FixedFluxPressure and hp = hydrostatic pressure.

Boundary	Zone	Type	α	k	ω	u^a	u^b	p	Θ (for kinetic theory)
Top	1	patch	zG	zG	zG	zG	zG	zG	zG
Bottom	2	wall	zG	zG	zG	fV, u^a =0	fV, u^b =0	fFP	zG
Inlet (flow)	3	patch	1D profile	fV, $k = 1 \times 10^{-4}$	zG	1D profile	1D profile	zG	fV, $k = 1 \times 10^{-6}$
Inlet (sed)	4	wall	zG	fV, $k = 1 \times 10^{-12}$	zG	fV, u^a =0	fV, u^b =0	zG	zG
Outlet (flow)	5	patch	zG	zG	zG	dM	dM	hp	zG
Outlet (sed)	6	patch	zG	zG	zG	zG	zG	zG	zG

the bed. This relationship highlights the interdependence of bed shear dynamics and localised erosion processes within the studied hydraulic environment. Ning, Li, and Li [64], through their numerical investigation into the effects of spur dike spacing on local scour and flow dynamics, identified bed shear stress as a principal factor governing the scouring process. Their findings indicate that elevated initial shear stress is instrumental in establishing the maximum scour depth, with subsequent adjustment of the bed leading to a reduction in shear stress within the scoured region. The study further demonstrates a significant positive Pearson correlation between scour depth and shear stress. Furthermore, the highest shear stress occurs in proximity to the spur dike head, resulting in pronounced erosion at this location, which typically coincides with the point of maximum scour depth.

4.5. Comparison between numerical simulation and scour depth predictive model results

A comparison is made between scour depth results of the present numerical study and the scour depth predictive model of Jayaratne et al. [14], defining sediments with coefficient of permeability (ms^{-1}) ranging from 10^{-4} to 10^{-3} (Eq. (8)).

$$\frac{D_s}{H_{d2}} = \lambda \left[exp\left(- \frac{\sqrt{H_{d2}}}{2.5\lambda\sqrt{h}\, sin\theta_2} \right) \right] \Big\} \; h > H_{d2} \tag{8}$$

where, D_s is the scour depth, H_{d2} is the height of the structure measured at the landward side (m), and $\lambda = 0.85$, is the fitted coefficient, h is the inundation height which is in terms of flow velocity (m), and θ_2 is the angle of the leeward slope. The experimental scour depth values, and the scour depth values obtained from the numerical study were plotted against the scour depth predictive model depicted in Fig. 15.

The predictive model for tsunami-induced scour depth was formulated based on field survey data collected in the aftermath of the 2011 Tohoku Tsunami. Experimental results were subsequently utilised to validate this model. The model proposes a resilient coastal dike structure designed to mitigate landward toe scour. This recommendation is consistent with the sea dike design approach of a landward face outlined in Zhu, Linham and Nicholls [65], as well as the coastal dike design proposed by Kato et al. [66]. Although the numerical simulations exhibited considerable deviation from the experimental measurements, it is noteworthy that the Realizable k-ε turbulence model was exclusively employed within the two-dimensional RANS framework. Despite these variations, the numerical data demonstrated a reasonable agreement with the predictive model.

A statistical measure, the root mean square error (RMSE), was applied to measure the concentration of the numerical data around the tsunami-induced scour model is as follows.

$$\mathrm{RMSE} = \sqrt{\frac{1}{n}\sum_{i=1}^{n}(y_i - \hat{y}_i)^2} \tag{9}$$

where y_i is observed value, $\hat{y}_i$ is predicted value, n is the number of data points. An acceptable RMSE value of 0.113 was calculated from the numerical model results (Table 9), compared to a lower RMSE value of 0.04 determined from the experimental data given in Abimbola [54].

5. Conclusions

The paper addresses a problem in coastal engineering widely identified by the researchers following the 2011 Tohoku Tsunami. After the catastrophic event, it was found out from the post tsunami field surveys that about 50 % of the destruction to the coastal defences was a result of scour failure at their landward toe. This study explores the classical turbulence modelling approach of the failure behind three different

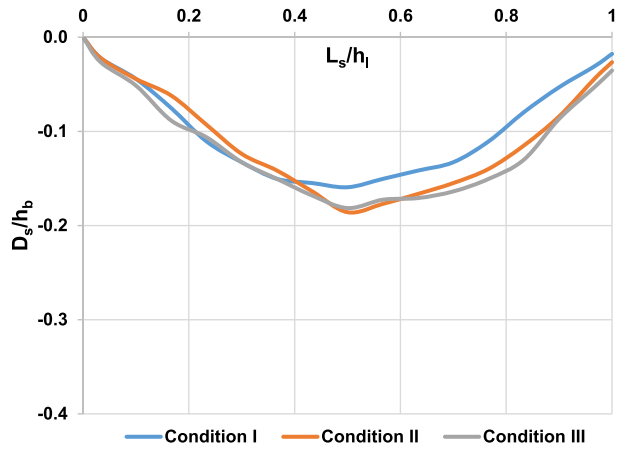

a. Scour profile for model dike A

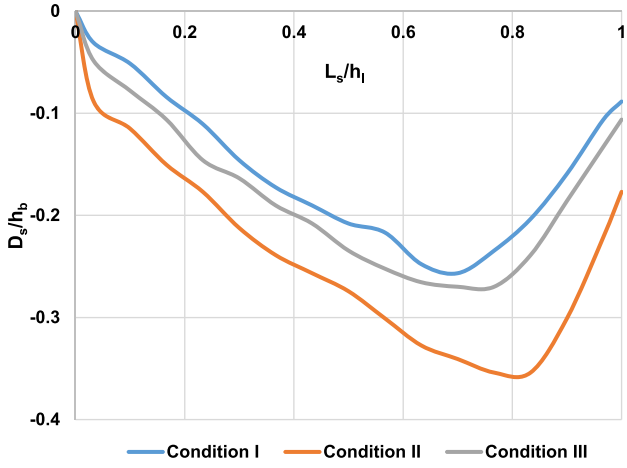

b. Scour profile for model dike B

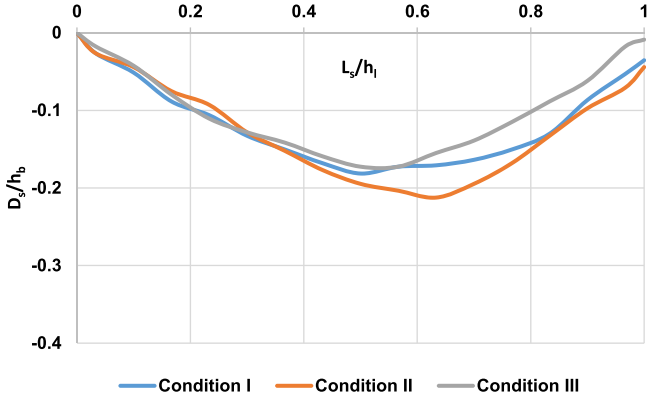

c. Scour profile for model dike C

Fig. 13. Scour profiles behind three tested model dikes under three hydraulic conditions, obtained by SedFoam 2.0.

coastal dike geometries and the correlation with a well-established tsunami-induced scour depth predictive model.

The total wave pressure over the faces of the three model dikes, i.e. seaward slope, crest and landward slope were measured using the numerical analysis. The statistical analysis of the numerical data reveals acceptable agreement with the maximum overflowing pressure values given by Mizutani and Imamura [59] model, which is fundamental to the principal hypothesis of the tsunami-induced scour depth predictive model. The numerical configuration was benchmarked against the experimental arrangement reported by Lobovsky et al. [57] to assess the validity of the computational framework and the simulated wave pressure results. The findings suggest that the application of the two-dimensional RANS modelling approach for dam-break flow predictions across different spatial domains should be undertaken with caution.

Further, it was found out from the study that when the slope of the dike is highest, the pressure decline between the seaward toe and landward toe increases. It was also found out from the study when the pressure in the landward toe of the dike increases, it results in increased shear stress in the region. When the shear increases, it increases the scouring in the landward side of the dike.

A two-phase flow solver named "SedFoam-2.0″ developed by Chauchat et al. [60], was employed to study the hydro-sedimentary characteristics in the leeward of the three model dikes. The study highlights that the integration of SedFoam-2.0 with RANS modelling provides an effective framework to simulate hydro-sedimentary dynamics under tsunami-like conditions. This coupling allows for a deeper understanding of the interaction between fluid flow and sediment transport mechanisms, which is critical for improving the resilience of coastal defence structures.

The present results lead to reveal a direct relationship between the shear stress, the maximum scour depth and its horizontal location from the landward toe. Also, the RMSE was used to compare the scour depths obtained from the present study and the predictive model of Jayaratne et al. [14], and the comparison results showed a good agreement. It is found that scour depths of the numerical study shows lower values compared to the experimental data and this was due to the fact that lower overflowing wave pressures generated from the numerical model. This might be because of the conditions that might have been set when the parameters for the numerical analysis were fed.

To address these discrepancies, future studies could explore the impact of refining boundary conditions in numerical models and incorporating site-specific parameters more comprehensively. Additionally, field-scale validation of numerical predictions could offer critical insights into the real-world applicability of the models used in this study.

Since the realizable k-ε turbulence model was applied in this study, the turbulence effect can be further investigated using other similar models. For the present study, 2D numerical computations with a two-phase solver have been used. *Future work could expand this framework to employ three-dimensional simulations, which would allow for a more nuanced analysis of turbulence and scour dynamics.* A new three-phase solver that would account for the air-water-sand interaction could be developed to fully capture and explore the tsunami-induced scour development process.

The findings of this study underscore the importance of continued research into the coupling of advanced numerical modelling techniques with predictive scour models. Such efforts are crucial for enhancing the design and implementation of coastal defence systems, particularly in regions vulnerable to extreme tsunami events.

CRediT authorship contribution statement

Ravindra Jayaratne: Writing – review & editing, Supervision, Resources, Project administration, Funding acquisition, Conceptualization. **Adewale Abimbola:** Writing – original draft, Visualization, Validation,

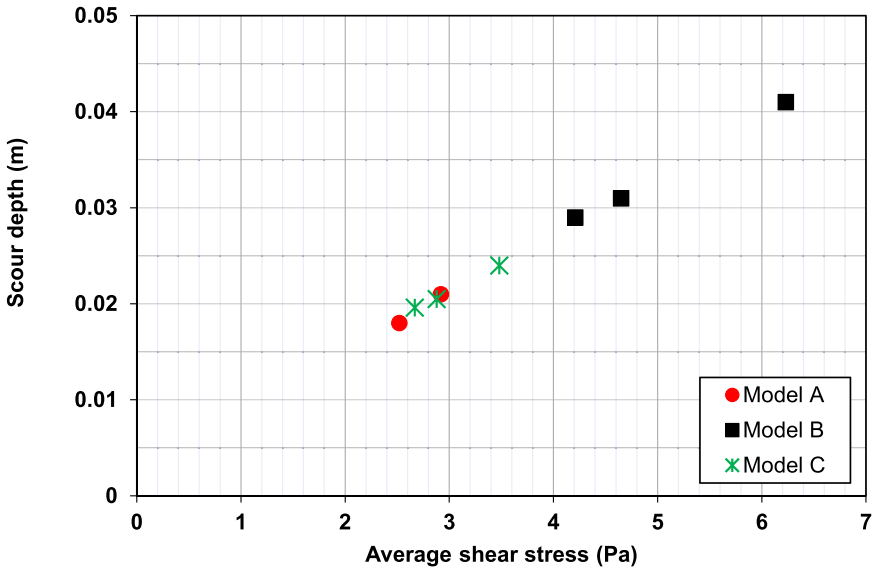

Fig. 14. Comparison between average shear stress and maximum scour depths derived from results of SedFoam 2.0.

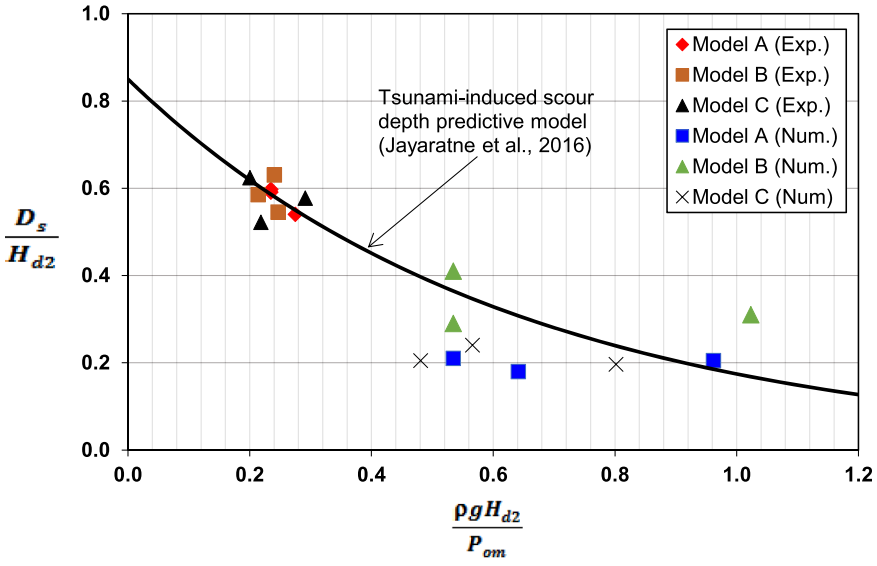

Fig. 15. Variation of non-dimensional scour depth and maximum overflowing wave pressure for both laboratory (Exp.) and numerical (Num.) investigations [$\frac{D_s}{H_{d2}}$ = non-dimensional scour depth and $\frac{\rho g H_{d2}}{P_{om}}$ = non-dimensional overflowing pressure, where P_{om} is maximum overflowing pressure].

Table 9
Comparison of root-mean-square errors of scour depth predictive model and ANSYS numerical model.

Dike geometry type	$\hat{X} = \frac{\rho g H_{d2}}{P_{om}}$ (Numerical data)	y_i (Numerical data)	$\hat{y}_i$ (Model data)	$(y_i - \hat{y}_i)^2$
	0.641	0.180	0.305	0.0156
A	0.534	0.210	0.361	0.0228
	0.962	0.205	0.182	0.000529
	0.534	0.290	0.361	0.00504
B	0.534	0.410	0.361	0.00240
	1.023	0.310	0.165	0.0210
	0.481	0.205	0.394	0.0357
C	0.566	0.240	0.344	0.0108
	0.802	0.196	0.236	0.00160

$\sum = 0.115$

$RMSE = \sqrt{\frac{0.115}{9}} = 0.113$

Methodology, Formal analysis. **Nilakshan Balasubramaniam:** Writing – original draft, Visualization, Software. **Mohammad Tabasi:** Writing – review & editing, Visualization, Formal analysis, Data curation.

Declaration of competing interest

The authors declare that they have no known competing financial interests or personal relationships that could have appeared to influence the work reported in this paper.

Data availability

Data will be made available on request.

References

[1] A.C. Cheng, A. Suppasri, M. Heidarzadeh, B. Adriano, C.T. Chua, F. Imamura, Tsunami wave characteristics in Sendai Bay, Japan, following the 2016 Mw 6.9

Fukushima earthquake, Ocean Eng. (2023), https://doi.org/10.1016/j.oceaneng.2023.115676.
[2] M. Heidarzadeh, A.R. Gusman, T. Ishibe, R. Sabeti, J. Šepić, Estimating the eruption-induced water displacement source of the 15 January 2022 Tonga volcanic tsunami from tsunami spectra and numerical modelling, Ocean Eng. (2022), https://doi.org/10.1016/j.oceaneng.2022.112165.
[3] M. Heidarzadeh, J. Šepić, T. Iwamoto, Long-duration storm surges due to 2023 successive UK storms Ciarán and Domingos: generation, field surveys, and numerical modelling, Ocean. Model. (Oxf) 194 (2025) 102487, https://doi.org/10.1016/j.ocemod.2024.102487.
[4] S. Waenpracha, P. Foytong, A. Suppasri, S. Tirapat, N. Thanasisathit, P. Maneekul, T. Ornthammarath, Development of fragility curves for reinforced-concrete building with masonry infilled wall under Tsunami, Adv. Civil Eng. 2023 (2023) 1–15.
[5] R. Jayaratne, N. Balasubramaniam, T. Kim, J. Bricker, Failure of seawalls due to tsunami-induced scour, in: *Coastal Engineering Proceedings*, 37, structures.72, 2023, https://doi.org/10.9753/icce.v37.structures.72.
[6] J. Li, X. Kong, Y. Yang, L. Deng, W. Xiong, CFD investigations of tsunami-induced scour around bridge piers, Ocean Eng. (2022), https://doi.org/10.1016/j.oceaneng.2021.110373.
[7] M.A. Rahman, N. Tanaka, N. Reheman, Experimental study on reduction of scouring and tsunami energy through a defense system consisting a seaward embankment followed by vertically double layered vegetation, Ocean Eng. (2021), https://doi.org/10.1016/j.oceaneng.2021.108816.
[8] R. Sabeti, M. Heidarzadeh, Numerical simulations of water waves generated by subaerial granular and solid-block landslides: validation, comparison, and predictive equations, Ocean Eng. (2022), https://doi.org/10.1016/j.oceaneng.2022.112853.
[9] F. Kato, S. Sato, H. Yeh, Large-scale experiment on dynamic response of sand bed around a cylinder due to tsunami, Coast. Eng. (2001) 1848–1859. *2000*.
[10] J.D. Bricker, M. Francis, A. Nakayama, Scour depths near coastal structures due to the 2011 Tohoku Tsunami, J. Hydraulic Res. 50 (6) (2012) 637–641.
[11] M. Heidarzadeh, T. Ishibe, A.R. Gusman, H. Miyazaki, Field surveys of tsunami runup and damage following the January 2024 Mw 7.5 Noto (Japan sea) tsunamigenic earthquake, Ocean Eng. (2024) 307, https://doi.org/10.1016/j.oceaneng.2024.118140.
[12] S.P. Tonkin, M. Francis, J.D. Bricker, Limits on coastal scour depths due to tsunami, Int. Effort. Lifeline Earthquake Eng. (2013) 671–678.
[13] D.J. McGovern, D. Todd, T. Rossetto, R.J.S. Whitehouse, J. Monaghan, E. Gomes, Experimental observations of tsunami induced scour at onshore structures, Coast. Eng. (2019) 152.
[14] M.P.R. Jayaratne, B. Premaratne, A. Adewale, T. Mikami, S. Matsuba, T. Shibayama, M. Esteban, I. Nistor, Failure mechanisms and local scour at coastal structures induced by Tsunami, Coastal Eng. J. 58 (4) (2016).
[15] T. Uda, A. Omata, Y. Yokoyama, S. Yamaki, Comparison between numerical calculation and experiment on tsunami run-up, Proc. Coast. Eng. Jpn. Soc. Civ. Eng. (JSCE) 34 (1987) 197–201.
[16] H. Moss, M. Heidarzadeh, R. Sabeti, Innovative coastal defence using rock bag revetments: preliminary physical modelling, Results. Eng. 26 (2025) 105151, https://doi.org/10.1016/j.rineng.2025.105151.
[17] T. Nakamura, Y. Kuramitsu, N. Mizutani, Tsunami scour around a square structure, Coastal Eng. J. 50 (2) (2008) 209–246, https://doi.org/10.1142/S057856340800179X.
[18] Kato, F., Tonkin, S., Yeh, H., Sato, S., & Torii, K.-I. 2001. *The grain-size effects on scour around a cylinder due to tsunami run-up* (Vol. 7).
[19] T. Yoshii, S. Tanaka, M. Matsuyama, Tsunami inundation, sediment transport, and deposition process of tsunami deposits on coastal lowland inferred from the Tsunami Sand Transport Laboratory Experiment (TSTLE), Mar. Geol. 400 (2018) 107–118.
[20] H.S. Kim, H. Chen, Three-dimensional numerical analysis of sediment transport around abutment in channel bend, in: Proceedings of the 34thInternal Conference on Coastal Engineering, ASCE, 2014.
[21] C. Baykal, B.M. Sumer, D.R. Fuhrman, N.G. Jacobsen, J. Fredsøe, Numerical investigation of flow and scour around a vertical circular cylinder, Philos. Trans. a Math. Phys. Eng. Sci. 373 (2033) (2015).
[22] F. Hongwei, W. Rodi, Three-dimensional mathematical model and its application in the neighbourhood of the three gorges reservoir dam in the Yangtze river, Acta Mechanica Sinica 18 (3) (2002) 235–243.
[23] N. Tofany, M.F. Ahmed, M. Mamat, M.L. Husain, Simulation of scouring in front of an impermeable vertical breakwater using the RANS-VOF numerical model, J. Environ. Sci. Technol. 7 (6) (2014) 314–325.
[24] M. Burkow, M. Griebel, A full three-dimensional numerical simulation of the sediment transport and the scouring at a rectangular obstacle, Comput. Fluids 125 (2016) 1–10.
[25] Z. Zhang, B. Shi, Numerical simulation of local scour around underwater pipeline based on fluent software, J. Appl. Fluid Mech. 9 (2) (2016) 711–718.
[26] N. Ahmad, H. Bihs, A. Kamath, A. Arntsen, Three dimensional CFD modelling of wave scour around side-by-side and triangular arrangement of piles with REEF3D, in: *Proceedings of the 8th International Conference on Asian and Pacific Coasts (APAC),* Procedia Engineering 116, 2015, pp. 683–690.
[27] B.M. Sreedhara, A. Sanooj, Manu, S. Mandal, Simulation of local scour around circular and round nosed bridge pier using reef3d, Int. J. Innovat. Res. Sci., Eng. Technol. 5 (9) (2016) 149–154.
[28] Li, G., L. Lang, and J. Ning. 2013. "3D numerical simulation of flow and local scour around a spur dike" *Proceedings of the 35th International Association for Hydro-Environment Engineering and Research (IAHR) World Congress,* Chengdu, China, 1: 239–247.
[29] A. Saponieri, M. Di Risio, D. Pasquali, N. Valentini, F. Aristodemo, G. Tripepi, D. Celli, M. Streicher, L. Damiani, Beach profile evolution infront of storm seawalls: a physical and numerical study, Proceed. 36thInt. Conf. Coastal Eng. 1 (36) (2018) 70. Paper.
[30] D. Roelvink, A. Reniers, A. van Dongeren, J. van Thiel de Vries, R. McCall, J. Lescinski, Modelling storm impacts on beaches, dunes and barrier islands, Coast. Eng. (2009), https://doi.org/10.1016/j.coastaleng.2009.08.006.
[31] S.K. Kang, J. Lee, Y.K. Kim, A. Khosronejad, Experimental and numerical study on the flow characteristics around spur dikes at different length-to-depth ratios, Adv. Water Resour. 175 (2023) 104428, https://doi.org/10.1016/j.advwatres.2023.104428.
[32] N. Balasubramaniam, R. Jayaratne, T. Kim, J. Bricker, Comparative assessment of plunging jet scour depth predictive formulae under variable soil moisture conditions, Coastal Eng. Proceed. 38 (2025) 59, https://doi.org/10.9753/icce.v38.papers.59, paper.
[33] M.I. Tortumluoglu, Y. Yasir, M. Dogan, A.O. Aksoy, Experimental investigation of equilibrium and temporal scour around the round head of the rubble mound breakwater in case of breaking and non-breaking waves, Ocean Eng. (2024) 312, https://doi.org/10.1016/j.oceaneng.2024.119285.
[34] C. Xu, Z. Huang, A laboratory study of wave-induced local scour at an emergent pile breakwater, Ocean Eng (2023), https://doi.org/10.1016/j.oceaneng.2023.113618.
[35] T. Yu, Y. Li, X. Chen, J. Tang, Experimental study on wave- and current-induced scour around an anti-deposition permeable breakwater, Ocean Eng. 257 (2022), https://doi.org/10.1016/j.oceaneng.2022.111565.
[36] Kjartan Gislason, Jørgen Fredsøe, B.Mutlu Sumer, Flow under standing waves, Coast. Eng. (2009), https://doi.org/10.1016/j.coastaleng.2008.11.002.
[37] A De Best, E.W. Bijker, Scouring of a sand bed in front of a vertical breakwater, Oceanogr. Literat. Rev (1971).
[38] J.W. Eckert, Design of toe protection for coastal structures, in: Coastal Structures '83. Proc. Conference, ASCE, New York, 1983.
[39] Lyndell Z. Hales, Erosion control of scour during construction, Techn. Report - US Army Engineer Waterways Experiment Station (1980). HL-80-3.
[40] Herbich J.B., and Ko S.C. 1968. "Scour of sand beaches in front of seawalls." In, 1: 622–43. https://doi.org/10.9753/icce.v11.40.
[41] Steven A. Hughes, Jimmy E. Fowler, Wave-induced scour prediction at vertical walls, Coastal Sediments '91 2 (1991).
[42] Irie, I., and K. Nadaoka. 1985. "Laboratory reproduction of seabed scour in front of breakwaters." *Proc. Int. Ninteenth Coastal Engineering Conf.* (Houston, USA). https://doi.org/10.9753/icce.v19.116.
[43] R. Jayaratne, A. Abimbola, N. Balasubramaniam, Experimental and numerical study of the hydrosedimentary dynamics on the landside of a coastal dike, in: *Coastal Engineering Proceedings*, 38: structures.126, 2025, https://doi.org/10.9753/icce.v38.structures.126.
[44] T. Sawaragi, Scouring due to wave action At the toe of permeable coastal structure, Coastal Eng. Proceed. (10) (1966) 60, https://doi.org/10.9753/icce.v10.60.
[45] B.M. Sumer, J. Fredsøe, Scour at the head of a vertical-wall breakwater, Coast. Eng. 40 (1) (2000) 59–87, https://doi.org/10.1016/S0378-3839(00)00006-5, 10.1016/S0378-3839(96)00024-52000Experimental Study of 2D Scour and Its Protection at a Rubble-Mound BreakwaterCoastal Engineering.
[46] M. Tabasi, J. Mitsui, T. Suzuki, S. Kubota, T. Tanaka, Investigation of morphological changes around breakwaters with different wave-dissipating concrete blocks using physical and numerical models, Coastal Eng. J. 67 (2) (2025) 335–349, https://doi.org/10.1080/21664250.2025.2476821.
[47] Xie, S.L. 1981. "Scouring patterns in front of vertical breakwaters and their influences on the stability of the foundations of the breakwaters".
[48] D. Myrhaug, H. Rue, A. Tørum, Tentative engineering approach to scour around breakwaters in random waves, Coast. Eng. (2004), https://doi.org/10.1016/j.coastaleng.2004.07.022.
[49] Díaz, D.D.O., and D.F. Hinz. 2015. "Performance of eddy-viscosity turbulence models for predicting swirling pipe-flow: simulations and laser-doppler velocimetry" arXiv:1507.04648 [physics.flu-dyn].
[50] X. Gao, H. Zhang, J. Liu, B. Sun, Y. Tian, Numerical investigation of flow in a vertical pipe inlet/outlet with a horizontal anti-vortex plate: effect of diversion orifices height and divergence angle, Eng. Applic. Computat. Fluid Mech. 12 (1) (2018) 182–194.
[51] B.U. Senturk, H.G. Guler, C. Baykal, Numerical simulation of scour at the rear side of a coastal revetment, Ocean Eng 275 (2023) 114092, https://doi.org/10.1016/j.oceaneng.2023.114092.
[52] T. Shih, W. Liou, A. Shabbir, Z. Yang, J. Zhu, A new k-ϵ eddy viscosity model for high Reynolds number turbulent flows, *Elsevier*Comput Fluids 24 (3) (1995) 227–238.
[53] Edited D.L. Youngs, The time-dependent multi-material flow with large fluid distortion, in: K.W. Morton, M.J. Baines (Eds.), Numerical Methods for Fluid Dynamics, Academic Press, New York, 1982, pp. 273–285. Edited.
[54] A. Abimbola, Wave Propagation and Scour Failure of Coastal Structures Due to tsunamis" PhD Thesis, Department of Engineering & Construction, University of East London, 2018.
[55] B.E. Launder, D.B. Spalding, The numerical computation of turbulent flows, Comput. Methods Appl. Mech. Eng. 3 (2) (1974) 269–289.
[56] T. Arimitsu, K. Ooe, K. Kawasaki, Evaluation method of tsunami wave pressure acting on land structure using 2D depth-integrated flow simulation, in: Proceedings of the Coastal Dynamics Conference, ASCE, 2013, pp. 466–480.

[57] L. Lobovsky, E. Botia-Vera, F. Castellana, J. Mas-Soler, A. Souto-Iglesias, Experimental investigation of dynamic pressure loads during dam break, J. Fluids. Struct. 48 (2014) 407–434.
[58] H. Hu, J. Zhang, T. Li, Dam-break flows: comparison between flow-3d, mike 3 fm, and analytical solutions with experimental data, Appl. Sci. 8 (12) (2018) 2456, https://doi.org/10.3390/app8122456.
[59] S. Mizutani, F. Imamura, Design of coastal structure including the impact and overflow on tsunamis, in: Proceedings of Coastal Engineering 49, JSCE, 2002, pp. 731–735.
[60] J. Chauchat, Z. Cheng, T. Nagel, C. Bonamy, T. Hsu, SedFoam-2.0: a 3D two-phase flow numerical model for sediment transport, J. Geoscientif. Model Develop. 10 (12) (2017) 4367–4392.
[61] G.H. Keulegan, Laws of turbulent flow in open channels, J. Res. Natl. Bur Stand. (1934) 21 (RP1151) (1938) 707–741.
[62] J.G. Duan, L. He, X. Fu, Q. Wang, Mean flow and turbulence around experimental spur dike, Adv. Water. Resour. 32 (2009) 1717–1725, https://doi.org/10.1016/j.advwatres.2009.09.004.
[63] J. Hou, L. Zhang, Y. Gong, D. Ning, Z. Zhang, Theoretical and experimental study of scour depth by submerged water jet, Adv. Mechan. Eng. 8 (12) (2016) 1–9, https://doi.org/10.1177/1687814016682392.
[64] J. Ning, G. Li, S. Li, Numerical simulation of the influence of spur dikes spacing on local scour and flow, Appl. Sci. 9 (2306) (2019), https://doi.org/10.3390/app9112306.
[65] Zhu, X., Linham, M.M. and Nicholls, R.J. 2010. Technologies for Climate Change adaptation - Coastal erosion and flooding. Danmarks Tekniske Universitet, Risø Nationallaboratoriet for Bæredygtig Energi. TNA Guidebook Series.
[66] F. Kato, Y. Suwa, K. Watanabe, S. Hatogai, Mechanisms of coastal dike failure induced by the great east Japan earthquake tsunami, in: Proceedings of the 33rdInternational Conference on Coastal Engineering, ASCE, 2012.